

ARTICLE

DOI: 10.1038/s41467-018-06141-0

OPEN

Two-site H_2O_2 photo-oxidation on haematite photoanodes

Yotam Y. Avital¹, Hen Dotan², Dino Klotz² , Daniel A. Grave², Anton Tsyganok², Bhavana Gupta¹, Sofia Kolusheva³, Iris Visoly-Fisher¹, Avner Rothschild²  & Arik Yochelis^{1,4} 

H_2O_2 is a sacrificial reductant that is often used as a hole scavenger to gain insight into photoanode properties. Here we show a distinct mechanism of H_2O_2 photo-oxidation on haematite ($\alpha\text{-Fe}_2\text{O}_3$) photoanodes. We found that the photocurrent voltammograms display non-monotonous behaviour upon varying the H_2O_2 concentration, which is not in accord with a linear surface reaction mechanism that involves a single reaction site as in Eley-Rideal reactions. We postulate a nonlinear kinetic mechanism that involves concerted interaction between adions induced by H_2O_2 deprotonation in the alkaline solution with adjacent intermediate species of the water photo-oxidation reaction, thereby involving two reaction sites as in Langmuir-Hinshelwood reactions. The devised kinetic model reproduces our main observations and predicts coexistence of two surface reaction paths (bi-stability) in a certain range of potentials and H_2O_2 concentrations. This prediction is confirmed experimentally by observing a hysteresis loop in the photocurrent voltammogram measured in the predicted coexistence range.

¹Department of Solar Energy and Environmental Physics, Swiss Institute for Dryland Environmental and Energy Research, Blaustein Institutes for Desert Research (BIDR), Ben-Gurion University of the Negev, 8499000 Midreshet Ben-Gurion, Israel. ²Department of Materials Science and Engineering, Technion – Israel Institute of Technology, 32000 Haifa, Israel. ³Ilse Katz Institute for Nanoscale Science and Technology, Ben-Gurion University of the Negev, 8410501 Be'er Sheva, Israel. ⁴Department of Physics, Ben-Gurion University of the Negev, 8410501 Be'er Sheva, Israel. Correspondence and requests for materials should be addressed to A.Y. (email: yochelis@bgu.ac.il)

Photoelectrochemical (PEC) water splitting is an elegant route to store radiant solar power in chemical bonds by producing hydrogen¹. Haematite ($\alpha\text{-Fe}_2\text{O}_3$) is an attractive model material for the photoanode in the PEC cell given its visible light absorption², abundance, non-toxicity, high catalytic activity for water oxidation³, and, most importantly, stability in alkaline solutions⁴. Recent advances in haematite photoanodes have led to significant progress in improving their performance, with most of the progress focused on enhancing the photocurrent, reaching over 4 mA cm^{-2} for champion haematite photoanodes^{5–8}. The photocurrent records were achieved at electrode potentials of over $1.4 V_{\text{RHE}}$ (Volts vs. the reversible hydrogen electrode)^{5–8}, which is well above the flat-band potential of haematite photoanodes ($0.3\text{--}0.4 V_{\text{RHE}}$)⁹. Enhancing the photocurrent and reducing the applied bias (potential) are required to compete with the efficiency of PV-powered electrolysis systems¹⁰. Achieving these goals would benefit from detailed understanding of the underlying processes that govern the photo-generation, recombination, and charge transfer at the semiconductor electrode|electrolyte interface^{9,11–15}.

PEC reactions, such as water splitting and other fuel production reactions, involve three components that give rise to physicochemical processes spanning a wide range of spatiotemporal scales^{16–18}. The first component is the semiconductor photoelectrode, where the light absorption, charge carrier generation, separation and transport toward the photoelectrode|electrolyte interface occur. Material properties that control these processes and competing processes that lead to charge recombination play a central role in the photoelectrode operation and performance. The second component is the electrolyte, which supplies the chemical reactants for the fuel production reaction and maintains the ionic conductivity required to close the electrical circuit between the electrodes. The third component is the photoelectrode|electrolyte interface, where the charge transfer reaction occurs (from electronic charges within the photoelectrode to ionic charges within the electrolyte). All three components are cross-linked by feedback loops that follow matter and charge conservation laws.

The oxygen evolution reaction which occurs at the photoanode|electrolyte interface is a complex four-electron process that requires multiple surface intermediates that facilitate interfacial charge transfer with the reactants from the electrolyte^{19,20}. On the other hand, those intermediates can also serve as recombination centres for photo-generated charge carriers²¹. Thus, surface intermediates display intriguing and rich dynamics that have a strong influence on the PEC performance of semiconductor electrodes^{14,22}, which on haematite photoanodes are still under debate^{23–25}. Numerous experimental and theoretical reports have suggested the existence of a stable $\text{Fe}=\text{O}$ intermediate species^{24–26}. The existence of this intermediate was recently confirmed by *operando* infrared spectroscopy²⁶. The formation of this long-lived intermediate is the first step in the multi-step water photo-oxidation process on haematite photoanodes²⁶, but it also serves as a centre for recombination of electrons and holes, which results in large overpotential and efficiency losses^{14,22}.

One way of suppressing the effects of surface recombination in order to study bulk processes within the photoanode is through the use of sacrificial reductants, such as H_2O_2 ²⁷. At high concentrations (typically about 0.5 M), H_2O_2 serves as a hole scavenger that collects the photo-generated holes much faster than the surface recombination reaction²⁸. Therefore, it provides an upper limit for the bulk-limited photocurrent. Consequently, H_2O_2 is mostly exploited at high concentrations to gain insights into photoanode properties, such as charge carrier collection and charge transfer efficiencies²⁷, and it is

often considered a surrogate substrate to assess the potential effectiveness of water oxidation co-catalysts^{29,30}. However, the mechanism by which H_2O_2 extracts the photo-generated holes remains elusive. The understanding of this mechanism may lead to rational design of photoanode|electrolyte interfaces and co-catalysts that enhance hole collection and reduce deleterious surface recombination in closely related processes, such as water photo-oxidation.

Here we study the H_2O_2 photo-oxidation mechanism on a model haematite photoanode. By combining experimental studies at different H_2O_2 concentrations in alkaline solution together with theoretical modelling of the reaction kinetics, we postulate that the overall H_2O_2 photo-oxidation reaction, $\text{H}_2\text{O}_2 + 2\text{h}^+ + 2\text{OH}^- \rightarrow 2\text{H}_2\text{O} + \text{O}_2$, begins with deprotonation of H_2O_2 to HOO^- in the alkaline solution³¹, followed by adsorption of HOO^- ions and interaction with adjacent surface intermediates ($\text{Fe}=\text{O}$) of the water photo-oxidation reaction²⁶. Thereby, the H_2O_2 photo-oxidation reaction involves a concerted interaction of two sites, as in Langmuir–Hinshelwood (LH) reactions³². The H_2O_2 photo-oxidation reaction competes with the water photo-oxidation reaction for the holes that arrive at the surface³³, and for the available surface sites and the intermediate species that facilitate both reactions. The consequences of this competition are unfolded by a nonlinear kinetic model that not only reproduced the experimental observations but also gave rise to unexpected predictions that were subsequently verified by further experiments. Unlike the linear models of water photo-oxidation on haematite that consider a multi-step reaction on a single surface site^{24–26,34,35}, as in Eley–Rideal (ER) reactions, our work suggests that splitting the reaction into two sites, as in LH reactions, enabled here by the presence of H_2O_2 in the electrolyte, gives rise to nonlinear behaviour and facilitates the collection of photo-generated holes by oxidized surface species that help to level the potential of the elementary steps involved in the reaction²⁰. The knowledge gained from this work may explain the behaviour observed for some common water oxidation co-catalysts based on cobalt^{36–38}, and be also used to rationally design co-catalysts that facilitate water oxidation via a two-site process²⁰.

In what follows, we first discuss photocurrent vs. potential voltammetry measurements and intensity-modulated photocurrent spectroscopy (IMPS) measurements carried out at different H_2O_2 concentrations ranging from 0 to 0.5 M in alkaline solution (1 M NaOH in deionized water). Secondly, we model and analyse the underlying surface reactions and calculate the photocurrent as a function of potential and H_2O_2 concentration. Thirdly, we show that the calculated results qualitatively reproduce the empirical observations and finally, we verify experimentally the model prediction that is related to hysteresis.

Results

PEC measurements. The photocurrent (j) vs. potential (U) voltammograms are shown in Fig. 1a; the measurements were done under white light-emitting diode (LED) illumination of 80 mW cm^{-2} (see Methods section for details) at H_2O_2 concentrations ranging from 0 to 500 mM in alkaline solution (1 M NaOH in deionized water). The photocurrent density, j , is the current measured under illumination after subtraction of the dark current (at the same potential), divided by the aperture area of the PEC cell. At low H_2O_2 concentrations (5 mM), the photocurrent voltammograms display three regions distinguished by their slope, i.e., weak increase in j with increased U up to point (i), rapid increase from point (i) to point (ii), and moderate increase from point (ii) onwards. At higher H_2O_2 concentrations (10 mM) j increases almost linearly with U , indicating that the flux of photo-generated holes arriving at the surface is proportional to

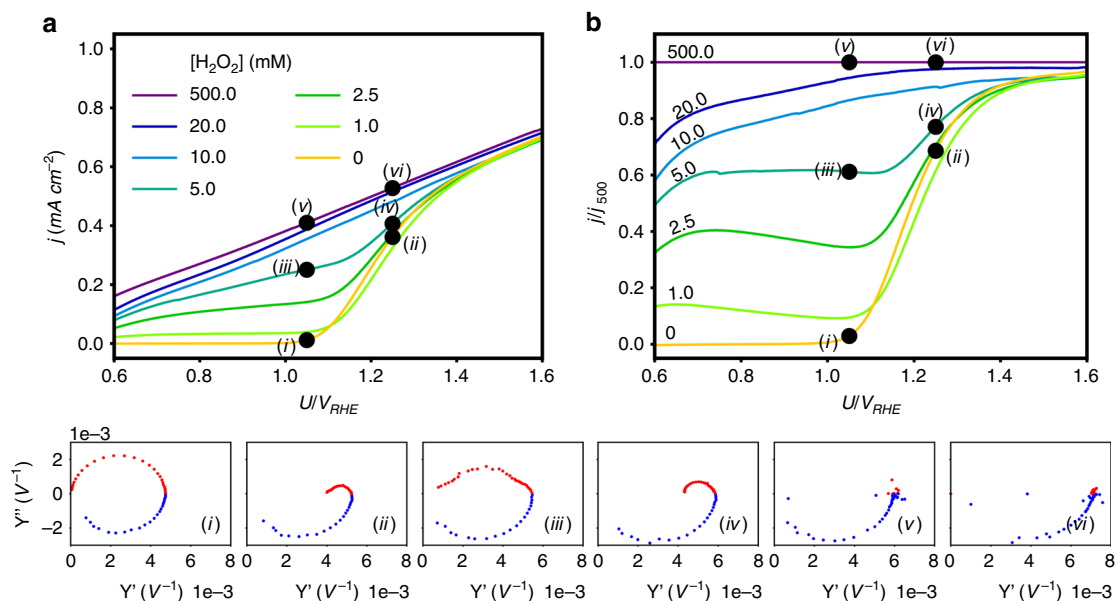


Fig. 1 Photocurrent voltammograms and intensity-modulated photocurrent spectra at varied H_2O_2 concentrations. **a** Photocurrent density as a function of the applied potential under white LED illumination (80 mW cm^{-2}) at different H_2O_2 concentrations as indicated in the legend. **b** Normalized photocurrent voltammograms obtained by dividing the photocurrent voltammograms in **a** by the photocurrent measured at $[\text{H}_2\text{O}_2]=500 \text{ mM}$, j_{500} . Bottom IMPS spectra correspond to: (i) $[\text{H}_2\text{O}_2]=0 \text{ mM}$, $U=1.05 V_{\text{RHE}}$, (ii) $[\text{H}_2\text{O}_2]=0 \text{ mM}$, $U=1.25 V_{\text{RHE}}$, (iii) $[\text{H}_2\text{O}_2]=5 \text{ mM}$, $U=1.05 V_{\text{RHE}}$, (iv) $[\text{H}_2\text{O}_2]=5 \text{ mM}$, $U=1.25 V_{\text{RHE}}$, (v) $[\text{H}_2\text{O}_2]=500 \text{ mM}$, $U=1.05 V_{\text{RHE}}$, (vi) $[\text{H}_2\text{O}_2]=500 \text{ mM}$, $U=1.25 V_{\text{RHE}}$

the applied potential. To distinguish the bias-dependent interfacial charge transfer at the photoanode|electrolyte interface from the bias-dependent hole flux from the bulk to the surface, the photocurrent voltammograms were normalized by the photocurrent obtained at the highest H_2O_2 concentration (500 mM), for which the surface reaction no longer limits the photocurrent²⁷. The normalized photocurrent voltammograms are depicted in Fig. 1b. They display an unexpected non-monotonous behaviour at low H_2O_2 concentrations (from 1 to 5 mM) wherein the normalized photocurrent first increases at low potentials, secondly decreases at moderate potentials, thirdly exhibits a steep rise at the onset potential around $1.1 V_{\text{RHE}}$, and finally converges with the water photo-oxidation current at about $1.5 V_{\text{RHE}}$.

To shed more light into the photocurrent behaviour at different H_2O_2 concentrations, IMPS measurements were carried out at potentials and H_2O_2 concentrations marked by points (i) to (vi) in Fig. 1a, b. The IMPS spectra of the complex photocurrent admittance, $Y(\omega) = j(\omega)/\Phi(\omega)$, where ω is the ac frequency and Φ is the light intensity, display two main features: upper (positive imaginary part) and lower (negative imaginary part) semicircles. The diameter of a lower semicircle corresponds to hole flux to the surface, whereas the diameter of the upper semicircle corresponds to surface recombination³⁹. In the absence of H_2O_2 in the electrolyte, the upper semicircle at low potentials (point (i)) is large, indicating strong surface recombination. Notably, the $Y(\omega)$ vanishes when $\omega \rightarrow 0$, indicating that all photo-generated holes arriving at the surface recombine with electrons such that an increase in light intensity does not lead to an increase in photocurrent. At higher potentials (point (ii)), the upper semicircle shrinks, indicating lower surface recombination as usually observed in haematite photoanodes in alkaline solution (without H_2O_2) at high potentials³⁹. The spectra obtained at a high H_2O_2 concentration (500 mM, points (v) and (vi)), display only the lower semicircle, whereas the upper semicircle disappears both at low and high potentials. This indicates that at high concentrations, H_2O_2 serves as an effective hole scavenger that suppresses surface recombination as expected²⁷. However, at

a low H_2O_2 concentration (5 mM, points (iii) and (iv)) surface recombination is strong at low potentials (point (iii)) and is suppressed at higher potentials (point (iv)), similarly to the situation without H_2O_2 (points (i) and (ii), respectively). These analogies indicate that in points (iii) and (iv), $Y(\omega)$ is dominated by water photo-oxidation rather than by H_2O_2 photo-oxidation. This implies that at low H_2O_2 concentrations, the photocurrent below the onset of water photo-oxidation is limited by the supply of H_2O_2 to the surface.

The transition from H_2O_2 -limited photocurrent at low potentials to H_2O_2 -independent photocurrent at high potentials implies a competition between H_2O_2 photo-oxidation and water photo-oxidation for the available holes, surface reaction sites and intermediate species³³. To test this hypothesis, we examine the effect of light intensity, which controls the photo-generation rate of excess charge carriers (holes), at a low H_2O_2 concentration of 2.5 mM. The results are shown in Fig. 2. The pronounced nonlinear behaviour observed at high light intensities becomes linear as the light intensity is decreased. This shows that at low light intensity, the photo-generation rate is low enough to enable hole scavenging even at low H_2O_2 concentrations. Another observation that supports our hypothesis is the saturation of the photocurrent density with increasing light intensities at potentials lower than $1.1 V_{\text{RHE}}$, which indicates that the photocurrent is limited by H_2O_2 rather than by the flux of photo-generated holes.

Modelling of the reaction kinetics. The experimental results presented in the previous section suggest that the fate of the photo-generated holes arriving from the bulk (where they are created) to the surface of the photoanode (where they vanish) involves different possible paths: H_2O_2 photo-oxidation, water photo-oxidation and recombination with electrons (surface recombination). The competition between these paths depends on control parameters such as the H_2O_2 concentration, light intensity and applied potential, thereby affecting the

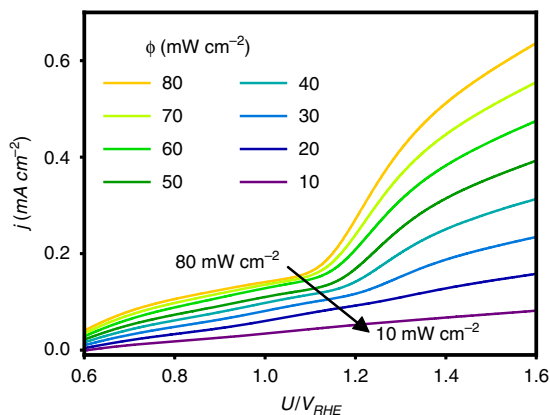
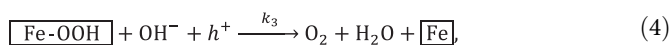
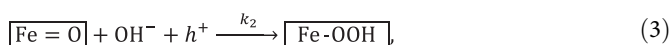
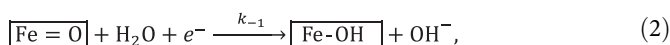
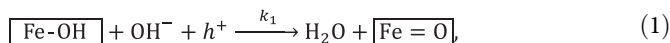


Fig. 2 Photocurrent voltammograms under different illumination intensities. For all measurements H_2O_2 concentration is at 2.5 mM

photocurrent. In order to understand the mechanisms of the respective reactions and the competition between them that determines the fate of the photo-generated holes, and thereby the performance of the photoanode, we construct a kinetic model. Our model extends the water photo-oxidation mechanism presented by Zandi and Hamann²⁶ and Zandi and co-workers⁴⁰, by adding additional steps that account for H_2O_2 photo-oxidation. The model yields kinetic equations, which we solve numerically in order to analyse the fate of the photo-generated holes as a function of the control parameters, aiming for qualitative agreement between the calculations and the experimental results in the entire parameter space examined. Since we aim for qualitative rather than quantitative agreement, our model is not so sensitive to the selection of the parameters (rate constants) in the kinetic equations, unlike multi-parametric fitting that aims for quantitative agreement by fitting the unknown parameters to reproduce the experimental results precisely. Instead, the essence of our model is in capturing the nonlinearity of the PEC kinetics that gives rise to the non-trivial behaviour observed in the experimental results presented in Figs. 1, 2. Therefore, the model depends on the phenomenological structure of the nonlinear kinetic equations rather than on the parameters within those equations.

We start with the widely accepted model of water photo-oxidation mechanism on haematite in alkaline solution^{26,40,41}:



where boxed ($\boxed{\dots}$) species correspond to surface intermediates and k_i are the respective rate constants. The reaction path from steps (1) to (5) is illustrated on the left side of Fig. 3. According to this mechanism, the water photo-oxidation current is given by the net summation of all the reaction rates, that is, the sum of the forward charge transfer rates (steps (1) and (3)–(5)) minus the backward reaction rate (step (2)). When both reactions (1) and (2) occur successively, their combination forms effectively a

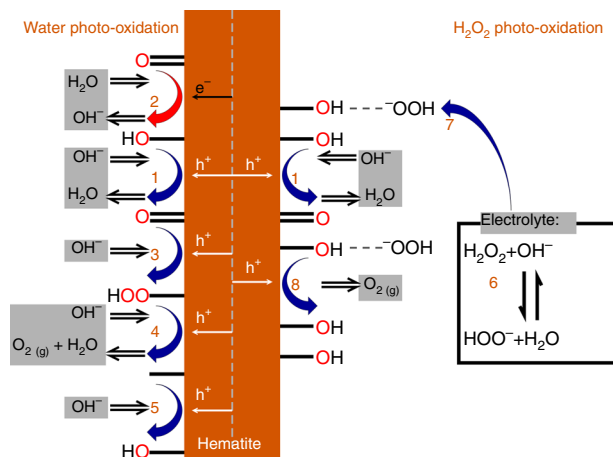
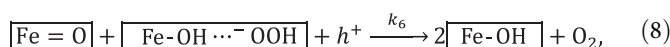
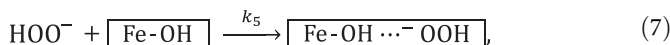
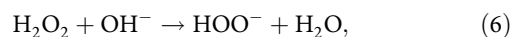


Fig. 3 Schematic illustration of water (left) and H_2O_2 (right) photo-oxidation reaction paths in alkaline solution. The former follows steps (1) to (5), whereas the latter follows steps (6) to (8) combined with step (1). In addition, the red arrow denotes the recombination reaction (2)

surface recombination step. It is noteworthy that steps (1)–(5) give rise to a set of linear kinetic equations, see Model equations and numerical computations in Methods.

Next, incorporating the H_2O_2 photo-oxidation reaction requires accounting for the following observations: (a) At low and intermediate potentials, the photocurrent depends on the H_2O_2 concentration, whereas at high potentials it coincides with the water photo-oxidation current (without H_2O_2), see Fig. 1a, b. This suggests that the H_2O_2 photo-oxidation reaction competes with the water photo-oxidation reaction³³. (b) Comparison of the IMPS spectra in points (i) and (iii) in Fig. 1 shows a deviation of the upper semicircle from a perfect shape in the presence of H_2O_2 in the electrolyte, which suggests that the H_2O_2 photo-oxidation reaction competes with the recombination reaction (step (2)). (c) Since the stable surface intermediate in the water photo-oxidation reaction is Fe=O ^{26,40,41}, it is expected that the competing step in the H_2O_2 photo-oxidation reaction should involve Fe=O intermediates. (d) In the presence of H_2O_2 in the electrolyte the photocurrent at low potentials is due to H_2O_2 photo-oxidation rather than water photo-oxidation. Under these conditions, the Fe=O intermediates are short-lived and the stable surface species is Fe-OH ²⁶. Thus, for H_2O_2 photo-oxidation to occur, an adsorption step that involves the long-lived Fe-OH species is expected to precede the step in which the anions interact with the Fe=O intermediates, as suggested in (c).

Accordingly, we postulate that the water photo-oxidation reaction (steps (1)–(5)) is complemented by the following steps to account for the H_2O_2 photo-oxidation reaction:



Step (6) describes the deprotonation reaction of H_2O_2 in the alkaline solution³¹, which occurs spontaneously since a pK_a of 11.7 for H_2O_2 deprotonation⁴² yields $[\text{HOO}^-]/[\text{H}_2\text{O}_2] \approx 100$ at $\text{pH} = 13.6$. Due to the fast nature of deprotonation reactions, step (6) is expected to occur much faster than the other steps, thus it does not affect the overall kinetics. Its product, HOO^- , is postulated to weakly (physically) adsorb to Fe-OH surface sites in

the next step, as described in step (7), in accordance with (d) above. Empirical evidence supporting this adsorption step was obtained by infrared spectroscopy (see Supplementary Figure 1 and related discussion in the Supplementary Information). It is also supported by previous works showing the adsorption of (non-deprotonated) H_2O_2 to Fe-OH surface sites in haematite⁴³ (and similarly in other transition metal oxides⁴⁴). Finally, step (8) postulates that the adsorbates from step (7) are oxidized by photo-generated holes coupled with proton transfer to adjacent Fe=O surface intermediates that were produced in step (1) of the water photo-oxidation reaction. Thus, step (8) represents a concerted interaction between two different surface species, one from the water photo-oxidation reaction and the second from H_2O_2 adsorption. It couples both reactions and gives rise to nonlinearity in the kinetic equations that depend on the concentration of the respective species (see Model equations and numerical computations in Methods for details). It is noted that the exact molecular identity of the surface species involved in the reaction is beyond the scope of this work, and it remains to be verified by spectroelectrochemical studies⁴⁵. However, this specific detail is not crucial to the results that follow, and alternative surface species may be considered without affecting the qualitative results of the analysis. The salient point is that the H_2O_2 photo-oxidation reaction mechanism involves a concerted interaction of two surface sites, as in LH reactions, consuming two holes and yielding an oxygen molecule. The postulated reaction path is schematically illustrated on the right side of Fig. 3.

To uncover the nonlinear nature of the elementary steps in the water and H_2O_2 photo-oxidation reactions that result in the measured non-monotonic photocurrents for certain H_2O_2 concentrations (see Fig. 1), we derive kinetic equations (see Model equations and numerical computations in Methods for details) and supplement them by the hole flux from the surface to the electrolyte that is given by the sum of the forward chemical reactions (1), (3)–(5), and (8):

$$k_1 p_4 \theta_{\text{Fe-OH}} \sigma_h + k_2 p_4 \theta_{\text{Fe=O}} \sigma_h + k_3 p_4 \theta_{\text{Fe-OOH}} \sigma_h + k_4 p_4 \theta_{\text{Fe}} \sigma_h + k_6 \theta_{\text{Fe-OH...OOH}} \theta_{\text{Fe=O}} \sigma_h = p_1, \quad (9)$$

where p_1 is the hole flux from the surface to the electrolyte⁴⁶, which in general depends on the illumination intensity and potential, and p_4 is the OH^- concentration in the electrolyte, which depends on the electrolyte composition, θ_x is the fractional surface coverage of species x , and σ_h corresponds to the surface

density of holes at reacting sites. It is useful to regard eq. 9 as the charge conservation constraint⁴⁶. In addition to the charge conservation constraint, we also employ a standard surface site conservation constraint:

$$\theta_{\text{Fe-OH}} + \theta_{\text{Fe=O}} + \theta_{\text{Fe-OOH}} + \theta_{\text{Fe}} + \theta_{\text{Fe-OH...OOH}} = 1. \quad (10)$$

Next, we define the normalized photocurrent that is related to the flux of holes across the surface (p_1) minus the flux of holes consumed by the surface recombination reaction (step (2)):⁴⁶

$$\frac{j}{j_{\text{max}}} = 1 - \frac{k_{-1} \theta_{\text{Fe=O}} p_2}{p_1}. \quad (11)$$

where p_2 is the electron density at the surface. We emphasize that this form regards only the reaction kinetics at the surface and it does not account for bulk processes that control the hole flux to the surface. From experiments, it is evident that p_1 is often potential dependent, but the dependence is relatively weak. For instance, in the results presented in Fig. 1 the dependence is essentially linear (see j_{500} in Fig. 1). In contrast to p_1 , p_2 displays strong dependence on the applied potential, $p_2 \propto \exp(-\varphi)$, where φ is dimensionless potential (see Model equations and numerical computations in Methods section for details). Thus Eq. (11) comprises an empirical normalization by p_1 (similarly to the normalization by j_{500} in Fig. 1b). Notably, the shape of the calculated voltammograms of the normalized photocurrent is essentially robust with respect to the potential dependence of p_1 , as shown here by comparing Fig. 4a, b in which p_1 is taken to be linearly proportional to U or independent of U , respectively. This implies a generic mechanism that is hidden in this physicochemical process that we unfold, in what follows, by using a bifurcation theory via keeping p_1 as constant for simplified analysis purposes, $p_1 = p_1^c$.

The qualitative similarity between the calculated curves in Fig. 4 and the experimental results in Fig. 1b is clearly evident. Specifically, the calculated curves capture the non-monotonous behaviour of the normalized photocurrent at low H_2O_2 concentrations and potentials below the onset of water photo-oxidation, and the convergence of the photocurrent at high potentials towards the water photo-oxidation limit. It is noted that the non-monotonous behaviour displayed by the cyan ($p_3 = 0.01$) curve in Fig. 4 emerges from the nonlinearity in the kinetic equations, as a result of the concerted interaction of two different surface sites as in step (8) above.

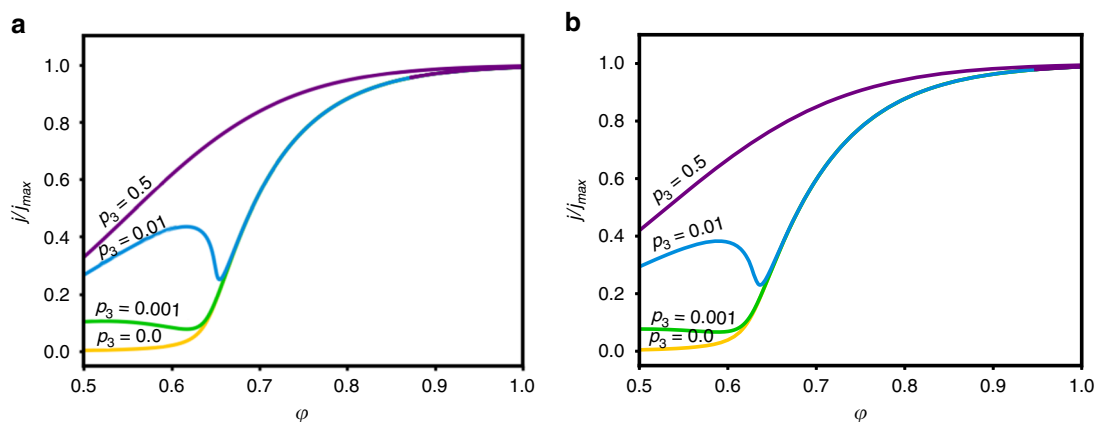


Fig. 4 Numerically computed normalized photocurrent voltammograms at different H_2O_2 concentrations (p_3). All the observables are dimensionless. The photocurrents are calculated for two cases in which p_1 is **a** with linear dependence on the applied potential, or **b** constant (see text and Model equations and numerical computations in Methods section for details)

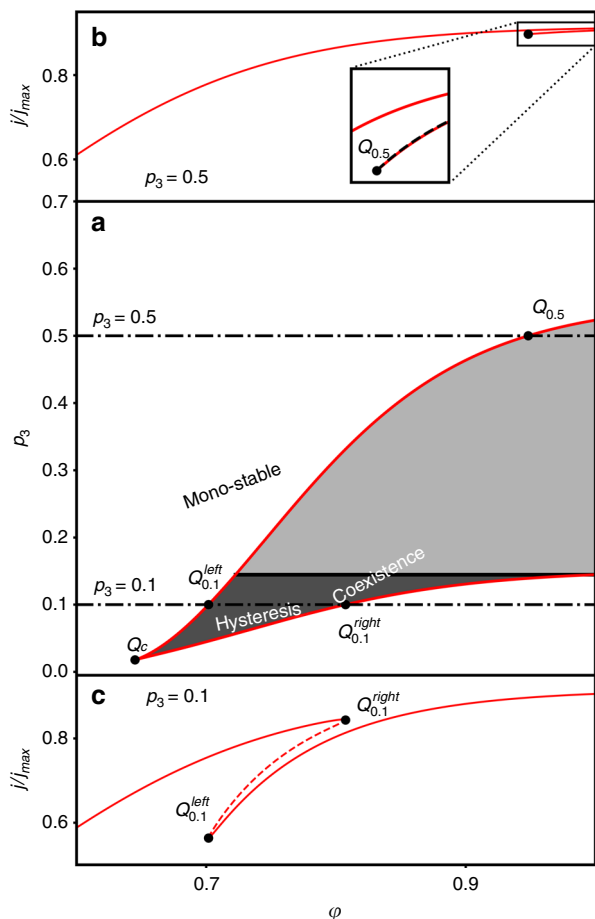


Fig. 5 Bi-stability and hysteresis. **a** Coexistence parameter space for the computed normalized photocurrent voltammograms showing the distinct regions of coexisting solutions. 2D projection of the manifold describing the computed normalized photocurrent voltammograms (i/i_{\max}) as a function of the applied dimensionless potential (ϕ) and H_2O_2 concentration (p_3), showing the coexistence (bi-stability) regime of the normalized photocurrent (the grey shaded area). The bold dashed line indicates the threshold between observable and non-observable hysteresis. **b, c** Simulated normalized photocurrent voltammograms at $p_3 = 0.5$ and 0.1 , respectively. Solid lines indicate stable solutions, whereas dashed lines indicate unstable ones. The transition points from stable to unstable solutions and vice versa in **b, c** are, respectively, marked in **a**

Bi-stability, competing kinetics and hysteresis. Analysis of the solutions shows that while for low H_2O_2 concentrations there is only one solution (mono-stable regime), above a certain threshold concentration there is a limited potential range in which stable solutions coexist, as shown in Fig. 5a, c. The coexistence of stable solutions implies that hysteresis in the photocurrent should be expected in this range of potentials and H_2O_2 concentrations. The hysteresis onset is at a generic cusp bifurcation⁴⁷ (marked by Q_c in Fig. 5a) in the two-parameter projection of the normalized photocurrent as a function of the potential (ϕ) and H_2O_2 concentration (p_3), see Fig. 5a. The shaded region between the curves in Fig. 5a is where coexistence of bi-stable solutions exists. Above $p_3 \approx 0.144$ (marked by the bold dashed line in Fig. 5a), although the coexistence persists, it cannot be observed experimentally because one of the stable solution branches spans the entire relevant potential range. In this case, an unstable solution connects the two stable solutions only at infinite potential, a known and universal (model independent) property of the cusp bifurcation⁴⁷. Thus, our calculations predict a stable unique behaviour

at low and high H_2O_2 concentrations, whereas at intermediate concentrations bi-stable solutions and hysteresis are expected (in a certain potential range). It is noted that additional calculations (not shown here) demonstrate the same qualitative behaviour with similar features of hysteresis and multiplicity of solutions (i.e., bi-stable regimes) over a wide range of parameters spanning orders of magnitude of the respective rate constants, confirming the robustness of our model predictions. Moreover, the simple ER mechanism typically used to describe water photo-oxidation on haematite photoanodes^{24,25,34,35} cannot yield such hysteresis because it lacks nonlinearity in the kinetic equations of its elementary steps (see Model equations and numerical computations in Methods for details).

The hysteresis predicted by the model calculations was validated by linear sweep voltammetry measurements, as shown in Fig. 6. Consistent with the model predictions, hysteresis was observed only at intermediate H_2O_2 concentrations (5 mM; Fig. 6b) but not at low and high concentrations (Fig. 6a, c, respectively). The hysteresis mechanism is consistent with the proposed reaction path (Fig. 3) through examination of the potential dependence (and therefore dependence on the potential sweep direction) of the distinct surface species involved in the reaction. Specifically, we focus on the evolution of the $\text{Fe}=\text{O}$, Fe-OH , and $\text{Fe-OH}\cdots\text{OOH}$ species. At low potentials, for example, $U = 0.6 \text{ V}_{\text{RHE}}$, the concentration of electrons at the surface is high (because the photoanode is donor-doped) and the recombination rate (step (2)) is fast, and therefore the surface is covered mostly by the long-lived Fe-OH and $\text{Fe-OH}\cdots\text{OOH}$ species, whereas the short-lived $\text{Fe}=\text{O}$ intermediates are minority species. Thus, the photocurrent at low potentials is dominated by the reaction path associated with the formation of $\text{Fe-OH}\cdots\text{OOH}$ adions with increasing potentials, that is, in the $0.8 \text{ V}_{\text{RHE}} \leq U \leq 1.3 \text{ V}_{\text{RHE}}$ range, the electron concentration at the surface decreases due to band bending, thereby prolonging the lifetime of the $\text{Fe}=\text{O}$ intermediates. Consequently, the surface concentration of $\text{Fe}=\text{O}$ increases, leading to comparable contributions to the photocurrent from both the water and H_2O_2 photo-oxidation reactions. At high potentials, $U \geq 1.3 \text{ V}_{\text{RHE}}$, the surface recombination becomes negligible and the surface is covered mostly by long-lived $\text{Fe}=\text{O}$ intermediates. If the potential is then swept in the opposite direction, that is from high to low potentials, the surface coverage of $\text{Fe}=\text{O}$ decreases progressively. Unlike during the potential sweep from low to high potentials, the time scale that is required to form a significant coverage of $\text{Fe-OH}\cdots\text{OOH}$ adions is much larger than in the reverse direction, consequently the H_2O_2 photo-oxidation reaction dominates. Thus, the different time scales that are associated with the evolution of different surface intermediates are manifested as hysteresis in the case of H_2O_2 photo-oxidation that involves concerted interaction of different intermediate species.

Discussion

The two-site interaction postulated here belongs to the LH class of surface reactions, where two different surface species mutually interact. This mechanism is inherently different from the single-site, multi-step process that accounts for the reported reaction mechanism of water photo-oxidation on haematite^{24–26,34,35}, as in ER reactions. Our two-site/LH reaction mechanism provides a favourable photo-oxidation path by splitting the charge transfer steps across two sites rather than the single-site/ER water photo-oxidation reaction, thereby helping to level the potential of the elementary steps involved in the reaction²⁰. In a broader context, the nonlinear photocurrent voltammograms observed at certain H_2O_2 concentrations (see Fig. 1) correspond to a class of systems exhibiting negative differential resistance, typical of competing

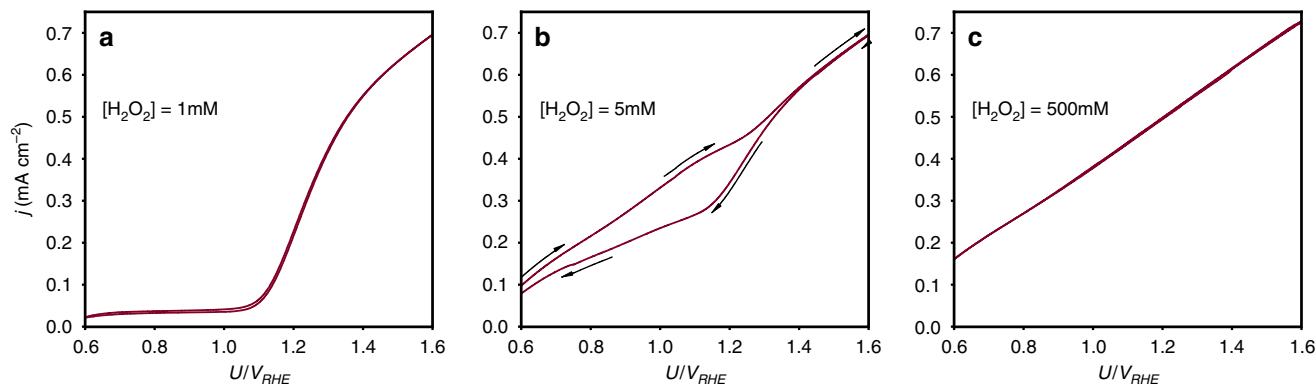


Fig. 6 Experimental realization of hysteresis. Forth and back linear sweep voltammetry scans at different H_2O_2 concentrations in alkaline solution (1 M NaOH) under white LED illumination of 80 mW cm^{-2} : **a** 1 mM, **b** 5 mM and **c** 500 mM. Hysteresis is observed only at $[\text{H}_2\text{O}_2]=5 \text{ mM}$. The arrows indicate the direction of potential sweep from low to high potentials and then back to low potentials

mechanisms with different time scales^{47,48}, as discussed above. Notably, the LH-like nature of the H_2O_2 photo-oxidation reaction bares similarity to catalytic CO oxidation⁴⁹, where bi-stability was observed and related to the generic character of LH reactions. This suggests that an appropriate spatiotemporal framework should be considered to account for concerted interaction between two sites, especially in cases where the simple single-site reaction scheme fails, as in the case of the H_2O_2 photo-oxidation reaction presented in this work.

It is noteworthy that two-site reactions on oxidized metal and metal oxide surfaces were previously suggested in the context of photocatalysis^{50,51} and water photo-oxidation^{20,32,52–56}. Particularly, hydroperoxide (HOO) adsorbed on metal sites participating in two-site LH-like reactions was suggested as part of the water oxidation mechanism on noble metals (Pt and Au) as well as Co_3O_4 ^{36,57}. Oxo-bridged and peroxo-bridged Fe dimers ($\text{Fe}^{\text{IV}}-\text{O}-\text{Fe}^{\text{IV}}$ and $\text{Fe}^{\text{IV}}-\text{O}-\text{O}-\text{Fe}^{\text{IV}}$) were found on haematite surface in alkaline solution, but were reported not to participate in water oxidation^{24,26}. The mechanism presented here, however, assumes the interaction of non-dimerized surface intermediates to form the O–O bond. The interaction of two non-dimerized surface intermediates in an LH-like mechanism has been suggested by Bockris¹⁹ to take part in the water oxidation mechanism. Such a mechanism was indeed reported for water photo-oxidation on haematite at high light intensities and high potentials, where the photocurrent saturates⁵⁸. The behaviour was attributed to conditions where the hole flux to the surface is high enough to allow the oxidation of nearest-neighbour sites, thereby reducing the surface recombination, consistent with our conclusion.

Given the ability of H_2O_2 to act as a hole scavenger, it often serves as a surrogate substrate that can be used to assess the effectiveness of co-catalysts for water photo-oxidation^{29,30}. Thus, understanding the mechanism by which H_2O_2 extracts photo-generated holes may further provide insight into the effect of water oxidation co-catalysts on haematite photoanodes (and possibly other photoanode materials) and assist in rational design of better performing co-catalysts. In this context, it has been reported that sub-monolayer coverage of cobalt on haematite photoanodes has improved their water photo-oxidation performance, with no further enhancement as a result of additional co-catalyst loading³⁶. Another study reported that the kinetic bottleneck that limits the water photo-oxidation performance of haematite photoanodes decorated with cobalt-phosphate (Co-Pi) water oxidation co-catalyst overlayers is effectively suppressed by sparse deposition on the haematite surface³⁷. Trivial assignment of the detrimental effect observed with thicker layers to parasitic

light absorption within the co-catalyst overlayer⁵⁹ was ruled out in this case by comparing back and front illumination measurements that were found to display similar trends³⁸. These counter-intuitive observations cannot be accounted for by the “adaptive junction” mechanism that often prevails in thicker ion-permeable co-catalyst overlayers^{60,61}, or by alternative mechanisms suggested by other researchers, such as the formation of a Schottky-type heterojunction at the haematite/Co-Pi interface⁶². Thus, the mechanism by which ultrathin/sparse co-catalyst overlayers improve the water photo-oxidation performance of haematite photoanodes remains elusive^{38,63,64}. The current work provides a possible insight to this enigma by considering that the water photo-oxidation reaction in the presence of sparse co-catalysts may proceed by a concerted interaction that involves two sites, one site from the photoanode and another site from the co-catalyst, similarly to the two-site H_2O_2 photo-oxidation reaction. Consistent with this view are the observations that ultrathin/sparse cobalt co-catalysts are more effective in enhancing water photo-oxidation at low potentials than at high potentials^{36,37}, indicating that the reaction proceeds via the co-catalyst at low potentials and via the haematite surface at high potentials³⁸. This is similar to the effect of H_2O_2 reported in this work, suggesting a possible link between the respective photo-oxidation schemes. In view of these examples, we conclude that a LH-like mechanism in PEC reactions may be a general phenomenon and should be considered as a possible route for enhanced collection of photo-generated charge carriers.

To conclude, this work shows that the photo-oxidation mechanism of hydrogen peroxide (H_2O_2) on haematite photoanodes proceeds via a concerted interaction between two different surface species, one from the water photo-oxidation reaction and the other from H_2O_2 adsorption. This two-site LH-like reaction occurs in parallel with the single-site ER-like water photo-oxidation reaction. Splitting the photo-oxidation reaction into two sites instead of one facilitates the collection of photo-generated holes by the oxidized species by helping to level the potential of the elementary steps involved in the reaction, thereby reducing kinetic barriers. Moreover, we show that the competition between the H_2O_2 and water photo-oxidation reactions for holes, intermediate species and surface sites, involves processes with different time scales, thereby giving rise to bi-stability phenomena that may lead to negative differential resistance and hysteresis in the photocurrent voltammograms. Our findings suggest that the concerted interaction of two surface intermediates should be considered as a possible path towards improving the photoelectrode performance. This may shed light

on the effect of ultrathin/sparse co-catalysts for water oxidation on haematite as well as other photoanodes.

Methods

Haematite photoanode. The samples consisted of a heteroepitaxial (110)-oriented Sn-doped (1%) haematite thin film photoanode (thickness ~30 nm) on Nb-doped SnO₂ (NTO) transparent electrode (thickness ~350 nm) deposited on an *a*-plane sapphire substrate. Details of the fabrication process and the microstructural characteristics of the photoanode can be found elsewhere⁶⁵.

PEC measurements. All measurements were conducted at ambient temperature in alkaline aqueous solutions (1 M NaOH in deionized water). For varying the H₂O₂ content, a 1 M NaOH + 0.5 M H₂O₂ solution was prepared in deionized water and diluted with 1 M NaOH in deionized water to reach the desired H₂O₂ concentrations. The pH of the electrolyte solution was kept fixed throughout the study. Linear sweep voltammetry measurements were carried out in a so-called cappuccino cell, as described in ref. ⁶⁶ with the photoanode serving as the working electrode, Pt mesh as the counter electrode and an Hg/HgO reference electrode in 1 M NaOH aqueous solution. The reference electrode has a potential of 0.930 V_{RHE}. The measurements were carried out with a Zahner Zennium electrochemical workstation equipped with a CIMPS system⁶⁷. The light source was a high power white LED (Zahner WLC02, 4300 K) with a maximum intensity of 120 mW cm⁻². The spectrum of this light source is shifted toward shorter wavelength than the AM1.5G solar spectrum, resulting in slightly higher photo-generation rate compared to proper solar simulators. To compensate for the spectral mismatch of our light source with respect to the AM1.5G solar spectrum, we reduced the light intensity to 80 mW cm⁻² instead of 100 mW cm⁻² in conventional solar simulators. Potential sweeps were performed by increasing the potential from 0.6 to 1.8 V_{RHE} and subsequently decreasing it back to 0.6 V_{RHE} with a sweep rate of 20 mV s⁻¹.

IMPS spectra were obtained by measuring both PEC impedance spectroscopy (PEIS) and intensity-modulated voltage spectroscopy (IMVS) at the corresponding operating point and then calculating the IMPS spectrum. This was done because of the better accuracy compared to direct IMPS measurement, as reported elsewhere³⁹. The frequency was scanned from 10 kHz to 0.7 Hz and the perturbation amplitude was 10 mV for PEIS and 20 mV for IMVS.

Spectroscopic characterization. For Fourier transformed infrared spectroscopy (FTIR) measurements, samples were soaked for 30 min in a NaOH (1 M) aqueous solution or in a NaOH (1 M) + H₂O₂ (0.5 M) aqueous solution, then washed in DI water (18 MΩcm) and dried in a gentle air flow. The FTIR spectra of the electrolyte solutions were recorded by a drop placed on an attenuated total reflection diamond crystal using a Nicolet 8700 FTIR spectrometer with a DTGS detector, with the background recorded on the clean diamond crystal. The spectra were recorded in the range from 4000 to 700 cm⁻¹, at 2 scanning resolution (0.24 cm⁻¹) and 36 scans. The FTIR spectra of the samples were recorded using an iN-10 FTIR microscope (Thermo Scientific) spectrometer equipped with a narrow-band liquid nitrogen-cooled MCTA detector. All single-beam spectra were measured against a background recorded from gold, with subtraction of the measured FTIR spectrum of the bare NTO/sapphire substrate. The spectra were recorded in the range from 4000 to 700 cm⁻¹, at 8 scanning resolution (1 cm⁻¹) and 128 scans; detection area was 100 × 100 μm². The FTIR data were collected using the OMNIC-Picta software.

Model equations and numerical computations. The rates of the reaction steps of the water and H₂O₂ photo-oxidation reactions, see eqs. (1)–(8), depend on the fractional surface coverage of species *x*, *θ_x*, which are dimensionless by definition. The units of the electron and hole surface densities, *σ_e* and *σ_h*, respectively, are given by their number surface density [*σ_e*] = [*σ_h*] = mol m⁻². The units of the rate constants are given according to the corresponding reaction orders: [*k*₁] = [*k*₂] = [*k*₃] = [*k*₄] = m³ mol⁻² s⁻¹, [*k*₅] = m³ mol⁻¹ s⁻¹, and [*k*₋₁] = [*k*₆] = m² mol⁻¹ s⁻¹, and thus the units of other parameters read as mol m⁻² s⁻¹ for *p*₁, mol m⁻² for

*p*₂ and mol m⁻³ for *p*₃ and *p*₄; *p*₁—the flux of photo-generated holes from the surface to the electrolyte; *p*₂—the electron density at the surface; *p*₃—the HOO⁻ concentration in the electrolyte (which is directly proportional to the concentration of H₂O₂); and *p*₄—the OH⁻ concentration in the electrolyte (related to the pH).

Introducing rescaled variables and parameters, *t* = *t*/τ, with τ = 1/*p*₄*k*₅, *p̂*₁ = *p*₁/*k*₆, *p̂*₂ = *p*₂/*σ*₀, with *σ*₀ = *k*₆⁻¹τ⁻¹ = *p*₄*k*₅/*k*₆, *p̂*₃ = *p*₃/*p*₄, *σ̂_h* = *σ_h*/*σ*₀, *k̂*₁ = *k*₁*p*₄/*k*₆, *k̂*₂ = *k*₂*p*₄/*k*₆, *k̂*₃ = *k*₃*p*₄/*k*₆, *k̂*₄ = *k*₄*p*₄/*k*₆, *k̂*₋₁ = *k*₋₁/*k*₆, we obtain a combined set of dimensionless kinetic equations for reactions (1)–(8). For ease of reading the hat signs were removed in what follows and in Table 1:

$$\frac{\partial \theta_{\text{Fe-OH}}}{\partial t} = k_{-1} p_2 \theta_{\text{Fe=O}} + k_4 p_4 \theta_{\text{Fe}} \sigma_h + 2 k_6 \theta_{\text{Fe=O}} \theta_{\text{Fe-OH}} \theta_{\text{OOH}} \sigma_h \quad (12)$$

$$- k_1 p_4 \theta_{\text{Fe-OH}} \sigma_h - k_5 p_3 (\theta_{\text{Fe-OH}} - \theta_{\text{Fe-OH}} \theta_{\text{OOH}}),$$

$$\frac{\partial \theta_{\text{Fe=O}}}{\partial t} = k_1 p_4 \theta_{\text{Fe-OH}} \sigma_h - k_{-1} p_2 \theta_{\text{Fe=O}} - k_6 \theta_{\text{Fe=O}} \theta_{\text{Fe-OH}} \theta_{\text{OOH}} \sigma_h - k_2 p_4 \theta_{\text{Fe=O}} \sigma_h, \quad (13)$$

$$\frac{\partial \theta_{\text{Fe-OOH}}}{\partial t} = k_2 p_4 \theta_{\text{Fe=O}} \sigma_h - k_3 p_4 \theta_{\text{Fe-OOH}} \sigma_h, \quad (14)$$

$$\frac{\partial \theta_{\text{Fe}}}{\partial t} = k_3 p_4 \theta_{\text{Fe-OOH}} \sigma_h - k_4 p_4 \theta_{\text{Fe}} \sigma_h, \quad (15)$$

$$\frac{\partial \theta_{\text{HOO}}}{\partial t} = k_5 p_3 (\theta_{\text{Fe-OH}} - \theta_{\text{Fe-OH}} \theta_{\text{OOH}}) - k_6 \theta_{\text{Fe=O}} \theta_{\text{Fe-OH}} \theta_{\text{OOH}} \sigma_h. \quad (16)$$

We note that our model addresses the working conditions of haematite photoanodes at high pH levels^{4–9}.

For analysis, we first solve numerically the model equations under the charge and site conservation constraints described by Eqs. (9) and (10), respectively, and examine all the possible steady-state solutions (fix points) to Eqs. (12) through (16). The equations have been numerically solved by continuation method using the publically available package AUTO⁶⁸. To determine the temporal stability of each steady-state solution, we linearize Eqs (12)–(16) about the fix points and solve the standard eigenvalue problem, while correlating the negative eigenvalues with stable solutions.

The dimensionless parameters *p*_{1,2,3,4} for Eqs (12)–(16) are unknown, and thus the results are qualitative in nature. Consequently, we compute and compare only the qualitative trends. The dimensionless rate constants were chosen such that their ratios are in accord with reported values for water photo-oxidation on haematite²⁴. The rate constants for the H₂O₂ photo-oxidation are rationalized in points (a) through (d) in the Results. The linear potential dependence of *p*₁ is chosen to be significantly smaller than 1, as most photo-generated holes do not arrive at the surface, see Table 1. The dimensionless OH⁻ concentration, *p*₄, was set to be equal to 1. We cannot derive a simple relation between *σ_h* and *p*₂, though such relation is expected from steps (1) and (2). The model parameters are summarized in Table 1. Additionally, we use a dimensionless potential scaled by *k_BT*/*q* and also normalized, i.e., *φ* = *U*/*U*_{sat}, where *U*_{sat} = 12 is the minimal potential for which all photocurrents for different H₂O₂ concentrations are considered to be saturate, *k_B* is Boltzmann constant, *T* is temperature, and *q* is elementary charge.

To test the validity of the LH-like mechanism proposed herein, a possible ER-like mechanism for H₂O₂ photo-oxidation was also considered. The alternative mechanism excludes reaction (7) and instead involves a direct interaction between HOO⁻ and Fe = O, implying that *k*₅*p*₃(*θ*_{Fe-OH} - *θ*_{Fe-OH}·*θ*_{OOH}) → 0 and *k*₆*θ*_{Fe=O} = *σ*_h*θ*_{Fe-OH}·*θ*_{OOH} → *k*₆*p*₃*σ*_h*θ*_{Fe=O}. The latter can then be combined with the linear *k*₂*p*₄*θ*_{Fe=O} term in Eq. (13), thereby removing the qualitative nonlinear nature of the solutions. Therefore, the resulting photocurrent based upon the ER-like mechanism fails to capture the non-monotonous behaviour observed in Fig. 1.

Table 1 Summary of dimensionless control parameters and the rate constants used for the numerical computation of the results presented in Fig. 4

Control parameter	Value	Interpretation	Rate constant	Value
<i>p</i> ₁	50 × exp(-4)	Hole flux to the electrolyte that is independent of the potential	<i>k</i> ₁	0.16
<i>p</i> ₁	1.2 × <i>φ</i> - 0.02	Hole flux to the electrolyte that is dependent on the potential	<i>k</i> ₋₁	2
<i>p</i> ₂	50 × exp(-12 × <i>φ</i>)	Electron density at the surface	<i>k</i> ₂	0.002
<i>p</i> ₃	∈ [0, 0.5]	[HOO ⁻]-[H ₂ O ₂]	<i>k</i> ₃	0.002
			<i>k</i> ₄	0.002
			<i>k</i> ₅	1
			<i>k</i> ₆	1

Data availability

All data generated or analysed during this study are included in this published article (and its Supplementary Information Files).

Received: 19 April 2018 Accepted: 8 August 2018

Published online: 09 October 2018

References

- Heller, A. Hydrogen-evolving solar cells. *Science* **223**, 1141–1148 (1984).
- Marusak, L. A., Messier, R. & White, W. B. Optical absorption spectrum of hematite, $\alpha\text{-Fe}_2\text{O}_3$, near IR to UV. *J. Phys. Chem. Solids* **41**, 981–984 (1980).
- Smith, R. D. L. et al. Photochemical route for accessing amorphous metal oxide materials for water oxidation catalysis. *Science* **340**, 60–63 (2013).
- Dias, P., Vilanova, A., Lopes, T., Andrade, L. & Mendes, A. Extremely stable bare hematite photoanode for solar water splitting. *Nano Energy* **23**, 70–79 (2016).
- Warren, S. C. et al. Identifying champion nanostructures for solar water-splitting. *Nat. Mater.* **12**, 842–849 (2013).
- Dotan, H. et al. Resonant light trapping in ultrathin films for water splitting. *Nat. Mater.* **12**, 158–164 (2013).
- Kim, J. Y. et al. Single-crystalline, wormlike hematite photoanodes for efficient solar water splitting. *Sci. Rep.* **3**, 2681 (2013).
- Guo, X., Wang, L. & Tan, Y. Hematite nanorods Co-doped with Ru cations with different valence states as high performance photoanodes for water splitting. *Nano Energy* **16**, 320–328 (2015).
- Sivula, K., Le Formal, F. & Grätzel, M. Solar water splitting: progress using hematite ($\alpha\text{-Fe}_2\text{O}_3$) photoelectrodes. *ChemSusChem* **4**, 432–449 (2011).
- Rothschild, A. & Dotan, H. Beating the efficiency of photovoltaics-powered electrolysis with tandem cell photoelectrolysis. *ACS Energy Lett.* **2**, 45–51 (2017).
- Iandolo, B., Wickman, B., Zorić, I. & Hellman, A. The rise of hematite: origin and strategies to reduce the high onset potential for the oxygen evolution reaction. *J. Mater. Chem. A* **3**, 16896–16912 (2015).
- Zandi, O. & Hamann, T. W. The potential versus current state of water splitting with hematite. *Phys. Chem. Chem. Phys.* **17**, 22485–22503 (2015).
- Shen, S., Lindley, S. A., Chen, X. & Zhang, J. Z. Hematite heterostructures for photoelectrochemical water splitting: rational materials design and charge carrier dynamics. *Energy Environ. Sci.* **9**, 2744–2775 (2016).
- Sivula, K. Metal oxide photoelectrodes for solar fuel production, surface traps, and catalysis. *J. Phys. Chem. Lett.* **4**, 1624–1633 (2013).
- Grave, D. A., Yatom, N., Ellis, D. S., Caspary Toroker, M. & Rothschild, A. The ‘rust’ challenge: on the correlations between electronic structure, excited state dynamics and photoelectrochemical performance of hematite photoanodes for solar water splitting. *Adv. Mater.* <https://doi.org/10.1002/adma.201706577> (2018).
- Kemppainen, E., Halme, J. & Lund, P. Physical modeling of photoelectrochemical hydrogen production devices. *J. Phys. Chem. C* **119**, 21747–21766 (2015).
- Zhang, X. & Bieberle-Hütter, A. Modeling and simulations in photoelectrochemical water oxidation: from single level to multiscale modeling. *ChemSusChem* **9**, 1223–1242 (2016).
- Pham, T. A., Ping, Y. & Galli, G. Modelling heterogeneous interfaces for solar water splitting. *Nat. Mater.* **16**, 401–408 (2017).
- Bockris, J. O. Kinetics of activation controlled consecutive electrochemical reactions: anodic evolution of oxygen. *J. Chem. Phys.* **24**, 817–827 (1956).
- Dau, H. et al. The mechanism of water oxidation: from electrolysis via homogeneous to biological catalysis. *ChemCatChem* **2**, 724–761 (2010).
- Shockley, W. & Read, W. T. Jr Statistics of the recombinations of holes and electrons. *Phys. Rev.* **87**, 835–842 (1952).
- Prérot, M. S. & Sivula, K. Photoelectrochemical tandem cells for solar water splitting. *J. Phys. Chem. C* **117**, 17879–17893 (2013).
- Klahr, B., Gimenez, S., Fabregat-Santiago, F., Hamann, T. & Bisquert, J. Water oxidation at hematite photoelectrodes: the role of surface states. *J. Am. Chem. Soc.* **134**, 4294–4302 (2012).
- Yatom, N., Neufeld, O. & Caspary Toroker, M. Toward settling the debate on the role of Fe_2O_3 surface states for water splitting. *J. Phys. Chem. C* **119**, 24789–24795 (2015).
- Braun, A. et al. The electronic, chemical and electrocatalytic processes and intermediates on iron oxide surfaces during photoelectrochemical water splitting. *Catal. Today* **260**, 72–81 (2016).
- Zandi, O. & Hamann, T. W. Determination of photoelectrochemical water oxidation intermediates on haematite electrode surfaces using operando infrared spectroscopy. *Nat. Chem.* **8**, 778–783 (2016).
- Dotan, H., Sivula, K., Grätzel, M., Rothschild, A. & Warren, S. C. Probing the photoelectrochemical properties of hematite ($\alpha\text{-Fe}_2\text{O}_3$) electrodes using hydrogen peroxide as a hole scavenger. *Energy Environ. Sci.* **4**, 958–964 (2011).
- Itoh, K. & Bockris, J. O. Thin film photoelectrochemistry: iron oxide. *J. Electrochem. Soc.* **131**, 1266–1271 (1984).
- Zhong, D. K., Choi, S. & Gamelin, D. R. Near-complete suppression of surface recombination in solar photoelectrolysis by “Co-Pi” catalyst-modified W: BiVO_4 . *J. Am. Chem. Soc.* **133**, 18370–18377 (2011).
- Abdi, F. F. et al. Efficient solar water splitting by enhanced charge separation in a bismuth vanadate-silicon tandem photoelectrode. *Nat. Commun.* **4**, 2195 (2013).
- Boehme, K. & Brauer, H. D. Generation of singlet oxygen from hydrogen peroxide disproportionation catalyzed by molybdate ions. *Inorg. Chem.* **31**, 3468–3471 (1992).
- Fang, Y.-H. & Liu, Z.-P. Mechanism and Tafel lines of electro-oxidation of water to oxygen on $\text{RuO}_2(110)$. *J. Am. Chem. Soc.* **132**, 18214–18222 (2010).
- Klotz, D., Grave, D. A., Dotan, H. & Rothschild, A. Empirical analysis of the photoelectrochemical impedance response of hematite photoanodes for water photo-oxidation. *J. Phys. Chem. Lett.* **9**, 1466–1472 (2018).
- Zhang, X., Klaver, P., van Santen, R., van de Sanden, M. C. M. & Bieberle-Hütter, A. Oxygen evolution at hematite surfaces: the impact of structure and oxygen vacancies on lowering the overpotential. *J. Phys. Chem. C* **120**, 18201–18208 (2016).
- English, N. J., Rahman, M., Wadnerkar, N. & MacElroy, J. M. D. Photo-active and dynamical properties of hematite (Fe_2O_3)-water interfaces: an experimental and theoretical study. *Phys. Chem. Chem. Phys.* **16**, 14445–14454 (2014).
- Kay, A., Cesar, I. & Grätzel, M. New benchmark for water photooxidation by nanostructured $\alpha\text{-Fe}_2\text{O}_3$ films. *J. Am. Chem. Soc.* **128**, 15714–15721 (2006).
- Zhong, D. K. & Gamelin, D. R. Photoelectrochemical water oxidation by cobalt catalyst (“Co-Pi”)/ $\alpha\text{-Fe}_2\text{O}_3$ composite photoanodes: oxygen evolution and resolution of a kinetic bottleneck. *J. Am. Chem. Soc.* **132**, 4202–4207 (2010).
- Carroll, G. M., Zhong, D. K. & Gamelin, D. R. Mechanistic insights into solar water oxidation by cobalt-phosphate-modified $\alpha\text{-Fe}_2\text{O}_3$ photoanodes. *Energy Environ. Sci.* **8**, 577–584 (2015).
- Klotz, D. et al. Empirical *in operando* analysis of the charge carrier dynamics in hematite photoanodes by PEIS, IMPS and IMVS. *Phys. Chem. Chem. Phys.* **18**, 23438–23457 (2016).
- Young, K. M. H., Klahr, B. M., Zandi, O. & Hamann, T. W. Photocatalytic water oxidation with hematite electrodes. *Catal. Sci. Technol.* **3**, 1660–1671 (2013).
- Hellman, A., Iandolo, B., Wickman, B., Grönbeck, H. & Baltrusaitis, J. Electro-oxidation of water on hematite: effects of surface termination and oxygen vacancies investigated by first-principles. *Surf. Sci.* **640**, 45–49 (2015).
- Goor, G., Glenneberg, J. & Jacobi, S. in *Ullmann’s Encyclopedia of Industrial Chemistry* Vol. 1, 131–139 (Wiley-VCH, Weinheim, Germany, 2007).
- Lin, S.-S. & Gurol, M. D. Catalytic decomposition of hydrogen peroxide on iron oxide: kinetics, mechanism, and implications. *Environ. Sci. Technol.* **32**, 1417–1423 (1998).
- Lousada, C. M., Johansson, A. J., Brinck, T. & Jonsson, M. Mechanism of H_2O_2 decomposition on transition metal oxide surfaces. *J. Phys. Chem. C* **116**, 9533–9543 (2012).
- Zhang, M. & Frei, H. Water oxidation mechanisms of metal oxide catalysts by vibrational spectroscopy of transient intermediates. *Annu. Rev. Phys. Chem.* **68**, 209–231 (2017).
- Klotz, D., Grave, D. A. & Rothschild, A. Accurate determination of the charge transfer efficiency of photoanodes for solar water splitting. *Phys. Chem. Chem. Phys.* **19**, 20383–20392 (2017).
- Krischer, K., Mazouz, N. & Grauel, P. Fronts, waves, and stationary patterns in electrochemical systems. *Angew. Chem. Int. Ed.* **40**, 850–869 (2001).
- Kalaev, D., Rothschild, A. & Riess, I. Negative differential resistance and hysteresis in $\text{Au}/\text{MoO}_3\text{-s}/\text{Au}$ devices. *RSC Adv.* **7**, 38059–38068 (2017).
- Imbihl, R. & Ertl, G. Oscillatory kinetics in heterogeneous catalysis. *Chem. Rev.* **95**, 697–733 (1995).
- Bahnemann, D. W., Hilgendorff, M. & Memming, R. Charge carrier dynamics at TiO_2 particles: reactivity of free and trapped holes. *J. Phys. Chem. B* **101**, 4265–4275 (1997).
- Draper, R. B. & Fox, M. A. Titanium dioxide photooxidation of thiocyanate: $(\text{SCN})_2^-$ —studied by diffuse reflectance flash photolysis—breaks. *J. Phys. Chem.* **94**, 4628–4634 (1990).
- Nakamura, R. & Nakato, Y. Primary intermediates of oxygen photoevolution reaction on TiO_2 (Rutile) particles, revealed by *in situ* FTIR absorption and photoluminescence measurements. *J. Am. Chem. Soc.* **126**, 1290–1298 (2004).
- Salvador, P. Mechanisms of water photooxidation at *n*- TiO_2 rutile single crystal oriented electrodes under UV illumination in competition with photocorrosion. *Prog. Surf. Sci.* **86**, 41–58 (2011).

54. Henderson, M. A. A surface science perspective on TiO₂ photocatalysis. *Surf. Sci. Rep.* **66**, 185–297 (2011).
55. Zhang, M., de Respinis, M. & Frei, H. Time-resolved observations of water oxidation intermediates on a cobalt oxide nanoparticle catalyst. *Nat. Chem.* **6**, 362–367 (2014).
56. Zhang, Y. et al. Rate-limiting O–O bond formation pathways for water oxidation on hematite photoanode. *J. Am. Chem. Soc.* **140**, 3264 (2018).
57. Rossmeisl, J., Logadottir, A. & Nørskov, J. K. Electrolysis of water on (oxidized) metal surfaces. *Chem. Phys.* **319**, 178–184 (2005).
58. Le Formal, F. et al. Rate law analysis of water oxidation on a hematite surface. *J. Am. Chem. Soc.* **137**, 6629–6637 (2015).
59. Trotochaud, L., Mills, T. J. & Boettcher, S. W. An optocatalytic model for semiconductor–catalyst water-splitting photoelectrodes based on in situ optical measurements on operational catalysts. *J. Phys. Chem. Lett.* **4**, 931–935 (2013).
60. Lin, F. & Boettcher, S. W. Adaptive semiconductor/electrocatalyst junctions in water-splitting photoanodes. *Nat. Mater.* **13**, 81–86 (2014).
61. Nellist, M. R., Laskowski, F. A. L., Lin, F., Mills, T. J. & Boettcher, S. W. Semiconductor–electrocatalyst interfaces: theory, experiment, and applications in photoelectrochemical water splitting. *Acc. Chem. Res.* **49**, 733–740 (2016).
62. Barroso, M. et al. The role of cobalt phosphate in enhancing the photocatalytic activity of α -Fe₂O₃ toward water oxidation. *J. Am. Chem. Soc.* **133**, 14868–14871 (2011).
63. Qiu, J. et al. Direct in situ measurement of charge transfer processes during photoelectrochemical water oxidation on catalyzed hematite. *ACS Cent. Sci.* **3**, 1015–1025 (2017).
64. Gamelin, D. R. Catalyst or spectator? *Nat. Chem.* **4**, 965–967 (2012).
65. Grave, D. A. et al. Effect of orientation on bulk and surface properties of Sn-doped hematite (α -Fe₂O₃) heteroepitaxial thin film photoanodes. *J. Phys. Chem. C* **120**, 28961–28970 (2016).
66. Deo Malviya, K. et al. Systematic comparison of different dopants in thin film hematite (α -Fe₂O₃) photoanodes for solar water splitting. *J. Mater. Chem. A* **4**, 3091–3099 (2016).
67. Zahner. CIMPS—Controlled Intensity Modulated Photo Spectroscopy <http://www.zahner.de/pdf/CIMPS.pdf>.33 (2011).
68. Doedel, E. J. et al. AUTO07p: continuation and bifurcation software for ordinary differential equations. <http://indy.cs.concordia.ca/auto> (2011).

Acknowledgements

This research was supported by the Ministry of National Infrastructures, Energy and Water Resources of Israel (grant no. 3-11430), the Ministry of Science and Technology of Israel (grant no. 3-14423), the European Research Council under the European Union's Seventh Framework programme (FP/200702013)/ERC (grant agreement no. 617516), and the Adelis Foundation. Y.Y.A. acknowledges support by the Kreitman

Fellowship, B.G. acknowledges the support of the Blaustein Centre for Scientific Cooperation's postdoctoral fellowship and D.A.G. acknowledges support by Marie-Sklodowska-Curie Individual Fellowship no. 659491. The experiments were performed using central facilities at the Technion's Hydrogen Technologies Research Laboratory (HTRL) supported by the Adelis Foundation and the Solar Fuels I-CORE program of the Planning and Budgeting Committee and the Israel Science Foundation (grant no. 152/11). We thank Maytal Caspary Toroker for useful comments on the manuscript.

Author contributions

A.Y. and H.D. conceived the idea. H.D., D.K., A.T., and B.G. designed and performed the experiments. S.K. performed the FTIR analysis. D.A.G. provided the hematite photoanodes. Y.Y.A., H.D., I.V.-F., A.R., and A.Y. designed the chemical modelling. Y.Y.A. and A.Y. performed the theoretical analysis and wrote the first draft. A.Y., I.V.-F. and A.R. supervised the research. All co-authors contributed to the analysis and to the writing of the final manuscript.

Additional information

Supplementary Information accompanies this paper at <https://doi.org/10.1038/s41467-018-06141-0>.

Competing interests: The authors declare no competing interests.

Reprints and permission information is available online at <http://npj.nature.com/reprintsandpermissions/>

Publisher's note: Springer Nature remains neutral with regard to jurisdictional claims in published maps and institutional affiliations.



Open Access This article is licensed under a Creative Commons Attribution 4.0 International License, which permits use, sharing, adaptation, distribution and reproduction in any medium or format, as long as you give appropriate credit to the original author(s) and the source, provide a link to the Creative Commons license, and indicate if changes were made. The images or other third party material in this article are included in the article's Creative Commons license, unless indicated otherwise in a credit line to the material. If material is not included in the article's Creative Commons license and your intended use is not permitted by statutory regulation or exceeds the permitted use, you will need to obtain permission directly from the copyright holder. To view a copy of this license, visit <http://creativecommons.org/licenses/by/4.0/>.

© The Author(s) 2018